Accepted Manuscript

Elastoplastic nonlinear FEM analysis of FGM shells of Cosserat type

Stanisław Burzyński, Jacek Chróścielewski, Karol Daszkiewicz, Wojciech Witkowski

PII: S1359-8368(18)31635-4

DOI: 10.1016/j.compositesb.2018.07.055

Reference: JCOMB 5822

To appear in: *Composites Part B*

Received Date: 22 May 2018

Revised Date: 19 July 2018

Accepted Date: 24 July 2018

Please cite this article as: Burzyński Stanisł, Chróścielewski J, Daszkiewicz K, Witkowski W, Elastoplastic nonlinear FEM analysis of FGM shells of Cosserat type, *Composites Part B* (2018), doi: 10.1016/j.compositesb.2018.07.055.

Title: Elastoplastic nonlinear FEM analysis of FGM shells of Cosserat type

Authors: Stanisław Burzyński, Jacek Chróścielewski, Karol Daszkiewicz, Wojciech Witkowski

Affiliation:

Gdańsk University of Technology, Faculty of Civil and Environmental Engineering,

Department of Mechanics of Materials,

80-233 Gdańsk, Narutowicza 11/12, Poland

Corresponding author:

Stanisław Burzyński

Gdańsk University of Technology, Faculty of Civil and Environmental Engineering,

Department of Mechanics of Materials,

80-233 Gdańsk, Narutowicza 11/12, Poland

Email: stanislaw.burzynski@pg.edu.pl

Phone: +48 58 347 17 55

1 Abstract

The paper is a continuation of [1] where the formulation of the elastic constitutive law for functionally graded materials (FGM) on the grounds of nonlinear 6-parameter shell theory with the 6^{th} parameter (the drilling degree of freedom) was presented. Here the formulation is extended to the elasto-plastic range. The material law is based on J_2 Cosserat plasticity and employs the well-known Tamura-Tomota-Ozawa (TTO) [2] mixture model with additional formulae for Cosserat material parameters. Formulation is verified by solving a set of demanding analyses of plates, curved and multi-branched shells, including geometry, thickness and material distribution variation parameter analyses.

Keywords: A. Functionally graded materials (FGMs), B. plastic deformation, C. Finite element analysis (FEA).

2 Introduction

The progress in material science and technology resulted in the so-called functionally graded materials (FGMs). The concept of FGMs with continuous change of the constituent materials in the given direction was proposed in [3]. A breakthrough in development of functionally graded materials was established by the works of Japanese scientists performed in the 80s and 90s [4]. The characteristic properties of FGMs are: no stress concentration aroused by discontinuity of material properties (typical for discrete composite layerwise material distribution [5]), resistance to heat, oxidation and corrosion typical of ceramics with simultaneous strength, ductility and toughness representative for metals [6]. The wide range of applications of FGMs in engineering results mostly from their thermal properties [7,8]. Most notably, the FGMs are applied in 2-dimensional models of structures such as plates e.g. [9–11] and shells e.g. [12–15]. For such structural elements, a lot of research, either analytical or numerical, was conducted towards better understanding of FGMs' behavior in various load and boundary conditions [16–19]. Stability analysis of FG sandwich beams and thin-walled functionally graded I-shaped beam was performed in [20] and [21], respectively. Rizov [22] evaluated the effect of material nonlinearity on delamination fracture in a functionally graded multilayered beam. Rational use of FGMs in thin-walled structures requires the knowledge about the stability, buckling loads and, last but not least, limit load capacity. Papers [23–25] provide a decent account of what has been done so far in these areas. Free vibration analysis of FGM plates and shells is topic of few recent papers eg. [26][27][28][29], results obtained there could be applied in aerospace design, one of possible FGM shells area of application.

This work presents the elastoplastic numerical analysis (based on Finite Element Method, FEM) of FGM shells. The elastoplastic analysis of FGMs was described for the first time in paper [30]. The Authors applied FE method to compute thermal residual stresses induced during cooling at graded ceramic-metal interfaces. Then, they investigated in [31] the influence of a gradient exponent and graded interlayer thickness on stress residual reduction. Aboudi and Pindera [32] studied thermo-inelastic response of functionally graded metal matrix composites

with nonuniform fiber spacing in the thickness direction. The influence of packing arrangements of metal and ceramic phases on the thermomechanical deformation and the local strains and stresses was analyzed in [33]. The material properties of FGM shell are usually computed using modified rule of mixtures (TTO model) proposed for metal alloys by Tamura et al. [2]. Determination method of TTO model parameters for FGMs was described in [34,35]. The method was based on inverse analysis and micro-indentation tests.

Jin et al [6] proposed an extension of the TTO model and presented the analysis of elastoplastic crack growth in the specimen with notch. The problem of elastoplastic deformation and residual thermal stresses induced in the fabrication process of FGM plates was analyzed in [7]. Baghani and Fereidoonnezhad [9] provided solution for circular plates loaded with arbitrary rotationally symmetric loads. The elasto-plastic behavior of FG circular plate under low velocity impact was investigated numerically and experimentally in [36,37]. Kalali et al [38] and Akis [12] discussed the elastoplastic behavior of functionally graded spherical vessels subjected to pressure. The elastoplastic analysis of FGM plate under termomechanical loading was performed in [11,39]. Huang and Han [5] compared their analytical solution with FEM solution for the functionally graded cylindrical shell subjected to axial compression. The stability of cylinders made of FGMs under various load conditions was studied in [18,40,41]. Xu et al. [42] and Kleiber et al. [43] analyzed elastoplastic buckling behavior of rectangular FGM plates. In contrast to the works described above, deformation of FGM plates with in-plane variation of material properties was described in [44]. Then, Amirpour et al. [8] developed elastoplastic damage model, discussed implementation and integration of constitutive relation using predictor-corrector scheme.

The aforementioned papers presented elastoplastic analysis of FGM plates, vessels and cylindrical shells. There seems to be a lack of research on elastoplastic behavior of shells with geometry other than flat and cylindrical. Hence, the aim of this paper is to provide several new numerical results for shells with orthogonal intersection as those used in thin-walled members.

The materially and geometrically nonlinear analysis will be performed for irregular functionally graded shells under mechanical loads.

The study is based on the shell theory that naturally includes the 6^{th} rotation parameter known as the drilling rotation. Theoretical aspects of the theory such as strong form of the initial-boundary value problem, jump conditions and weak forms were described for instance in [45–48]. One of the main aspects of the formulation is that the shell strain measures are not symmetric so that the theory falls into the category of materials with internal structure e.g. [49,50]. Particularly, here we deal with the case of Cosserat shell with rigid directors [51]. In addition, the theory is not limited by magnitude of displacements or rotations. Numerical analyses are based on the shell C^0 16-node finite elements CAM [52], with full Gauss-Legendre integration (4x4 point rule) of the element arrays in the element surface. The elements have 6 engineering degrees of freedom per node that makes them suitable tool for analysis of shells with various intersections undergoing finite rotations. Technically, the elements are based on Lagrange interpolation polynomials. However, the rotations are interpolated using special procedure as described in [53].

The elastoplastic constitutive law for the FGM 6-parameter shell is formulated in the course of the through-the-thickness integration of elastic Cosserat plane stress [49,54], using the concept of the first order shear deformation theory. Consequently the formulation is naturally endowed with characteristic length, since the Cosserat plane stress is assumed in each layer of the shell. Further assumptions pertaining the formulation of the material law are as follows (cf. e.g. [55,56]): additive decomposition of small elastoplastic strain rate and associative flow rule.

In our previous studies the elastic constitutive relation of FGM shells based on 2-D Cosserat plane stress was formulated with respect to the middle [57] and neutral [1] reference surface. The influence of: choice of material or neutral surface and characteristic length on the response of the shell was evaluated in paper [1]. Here, the elastoplastic constitutive model for functionally graded shells, consistent with used shell theory, is presented. At a single layer level plane stress Cosserat continua is assumed, with independent fields of in-plane translations and

drilling rotation. This results in non-symmetrical in-plane shear stresses and additional coupling stresses, taken into account in a natural way.

3 Elastoplastic constitutive relation

We briefly summarize the formulation of the FGM elastic constitutive relation as obtained in [1] in the range necessary to state the elastoplastic formulation.

3.1 Cosserat plane stress

As mentioned in previous section, assumption of Cosserat plane stress in each layer of the shell and then, integration through thickness is a natural and intuitive way of formulation material law in nonlinear 6-parameter shell theory. Cosserat continua and their various applications were described in many papers in recent times, e.g. [58][59][60][61]. In Cosserat media, not only position of point is defined, but also its orientation, thus at the given point displacements and rotations are independent. That leads to lack of symmetry stress and strains tensor and additional couple stress and curvature tensors are present. Details could be found e.g. in [62] along with reduction of 3D Cosserat continua to plane stress or strain cases.

Let $\mathbf{e}$ and stresses $\boldsymbol{\sigma}$ be the generalized strains defined at each lamina of the FGM shell

$$\begin{aligned}\mathbf{e}^{\mathrm{T}} &= \left\{\mathbf{e}_m \mid \mathbf{e}_d\right\} = \left\{e_{11}\ e_{22}\ e_{12}\ e_{21} \mid \kappa_{13}\ \kappa_{23}\right\},\\ \boldsymbol{\sigma}^{\mathrm{T}} &= \left\{\boldsymbol{\sigma}_m \mid \boldsymbol{\sigma}_d\right\} = \left\{\sigma_{11}\ \sigma_{22}\ \sigma_{12}\ \sigma_{21} \mid m_{13}\ m_{23}\right\}.\end{aligned} \tag{1}$$

The Cosserat material law between vectors $\mathbf{e}$ and $\boldsymbol{\sigma}$ is described by the following matrix [1]

$$\mathbf{C}^e = \left[\begin{array}{c|c} \mathbf{C}_{mm} & \mathbf{C}_{md} \\ \hline \mathbf{C}_{dm} & \mathbf{C}_{dd} \end{array}\right] = \left[\begin{array}{cccc|cc} Ea_1 & Ea_2 & 0 & 0 & 0 & 0 \\ Ea_2 & Ea_1 & 0 & 0 & 0 & 0 \\ 0 & 0 & G+\kappa & G-\kappa & 0 & 0 \\ 0 & 0 & G-\kappa & G+\kappa & 0 & 0 \\ \hline 0 & 0 & 0 & 0 & 2Gl^2 & 0 \\ 0 & 0 & 0 & 0 & 0 & 2Gl^2 \end{array}\right], \tag{2}$$

where $a_1 = \dfrac{1}{1-\nu^2}$, $a_2 = \nu a_1$, $\kappa(z) = G(z)\dfrac{N^2}{1-N^2}$. Here the symbol N, following [63], is referred to as the Cosserat coupling number. Equation (2) shows clearly the placement of the micropolar characteristic length *l*.

3.2 Strains in the shell space, stress and couple resultants

Employing the Reissner-Mindlin type kinematical assumption (the First Order Shear Deformation Theory, FOSDT) the membrane components of the strain vector $\mathbf{e}_m$ are computed from the following equation

$$\mathbf{e}_m = \boldsymbol{\varepsilon}_m + z\boldsymbol{\varepsilon}_b\,, \tag{3}$$

where $z \in [-h^-, +h^+]$ is the coordinate in the thickness direction $\boldsymbol{\varepsilon}_m$ and $\boldsymbol{\varepsilon}_b$ are the known strains at the shell reference surface

$$\boldsymbol{\varepsilon} = \{\varepsilon_{11}\ \varepsilon_{22}\ \varepsilon_{12}\ \varepsilon_{21} | \varepsilon_1\ \varepsilon_2 \| \kappa_{11}\ \kappa_{22}\ \kappa_{12}\ \kappa_{21} | \kappa_1\ \kappa_2\}^{\mathrm{T}} = \{\boldsymbol{\varepsilon}_m | \boldsymbol{\varepsilon}_s \| \boldsymbol{\varepsilon}_b | \boldsymbol{\varepsilon}_d\}^{\mathrm{T}}. \tag{4}$$

In (4) labels *m*, *s*, *b*, and *d* denote respectively: the membrane, shear, bending and drilling part. For the drilling part we assume that relation $\mathbf{e}_d = \boldsymbol{\varepsilon}_d$ holds in the shell space. It should be stressed that the FOSDT assumption (3) is not used in present formulation of 6-parameter theory anywhere else but only in postulated formulation of the material law in present approach.

The stress and couple resultants vector is defined correspondingly to (4) as

$$\mathbf{s} = \{N^{11}\ N^{22}\ N^{12}\ N^{21} | Q^1 Q^2 \| M^{11} M^{22} M^{12} M^{21} | M^1 M^2\}^{\mathrm{T}} = \{\mathbf{s}_m | \mathbf{s}_s \| \mathbf{s}_b | \mathbf{s}_d\}^{\mathrm{T}}. \tag{5}$$

The membrane, bending and drilling stress resultants are derived by integration of stresses through the shell thickness $z \in [-h^-, +h^+]$

$$\begin{aligned} \mathbf{s}_m &= \int_{-h^-}^{+h^+} \boldsymbol{\sigma}_m dz = \int_{-h^-}^{+h^+} [\mathbf{C}_{mm} \underbrace{(\boldsymbol{\varepsilon}_m + z\boldsymbol{\varepsilon}_b)}_{\mathbf{e}_m} + \mathbf{C}_{md} \underbrace{\boldsymbol{\varepsilon}_d}_{\mathbf{e}_d}] dz \\ &= \mathbf{A}_{mm}\boldsymbol{\varepsilon}_m + \mathbf{B}_{mb}\boldsymbol{\varepsilon}_b + \mathbf{C}_{md}\boldsymbol{\varepsilon}_d \end{aligned}, \tag{6}$$

$$\begin{aligned} \mathbf{s}_b &= \int_{-h^-}^{+h^+} \boldsymbol{\sigma}_m\, z dz = \int_{-h^-}^{+h^+} [\mathbf{C}_{mm}(z\boldsymbol{\varepsilon}_m + z^2\boldsymbol{\varepsilon}_b) + z\mathbf{C}_{md}\boldsymbol{\varepsilon}_d] dz \\ &= \mathbf{B}_{bm}\boldsymbol{\varepsilon}_m + \mathbf{E}_{bb}\boldsymbol{\varepsilon}_b + \mathbf{F}_{bd}\boldsymbol{\varepsilon}_d \end{aligned}, \tag{7}$$

$$\begin{aligned} \mathbf{s}_d &= \int_{-h^-}^{+h^+} \boldsymbol{\sigma}_d\, dz = \int_{-h^-}^{+h^+} [\mathbf{C}_{dm}(\boldsymbol{\varepsilon}_m + z\boldsymbol{\varepsilon}_b) + \mathbf{C}_{dd}\boldsymbol{\varepsilon}_d] dz \\ &= \mathbf{C}_{dm}\boldsymbol{\varepsilon}_m + \mathbf{F}_{db}\boldsymbol{\varepsilon}_b + \mathbf{H}_{dd}\boldsymbol{\varepsilon}_d \end{aligned}, \tag{8}$$

where the following arrays are defined

$$\mathbf{A}_{mm} = \int_{-h^-}^{+h^+} \mathbf{C}_{mm}\, dz\,,\ \mathbf{B}_{mb} = \mathbf{B}_{bm}^T = \int_{-h^-}^{+h^+} \mathbf{C}_{mm}\, z\, dz\,,\ \mathbf{C}_{md} = \mathbf{C}_{dm}^T = \int_{-h^-}^{+h^+} \mathbf{C}_{md} dz\,, \tag{9}$$

$$\mathbf{E}_{bb}=\int_{-h^-}^{+h^+}\mathbf{C}_{mm}z^2\,dz\,,\ \mathbf{F}_{bd}=\mathbf{F}_{db}^T=\int_{-h^-}^{+h^+}\mathbf{C}_{dm}z\,dz\,,\ \mathbf{H}_{dd}=\int_{-h^-}^{+h^+}\mathbf{C}_{dd}\,dz\,. \tag{10}$$

Note that the equations (6)-(10), unlike in our previous work [1], cannot be explicitly integrated. Instead, Gauss-Legendre or Gauss-Lobatto quadrature rule will be employed in the calculations. As far as the transverse shear is concerned the following equation is used, with α_s as the shear correction factor

$$\mathbf{C}_{ss}=\begin{bmatrix}G & 0\\ 0 & G\end{bmatrix},\qquad \mathbf{s}_s=\mathbf{D}_{ss}\boldsymbol{\varepsilon}_s=\alpha_s\int_{-h^-}^{+h^+}\mathbf{C}_{ss}\,dz\,\boldsymbol{\varepsilon}_s\,. \tag{11}$$

That is, the transverse shear stress-strain relation is treated as purely elastic in the present formulation. Finally, the structure of the constitutive relation is

$$\begin{Bmatrix}\mathbf{s}_m\\ \mathbf{s}_s\\ \mathbf{s}_b\\ \mathbf{s}_d\end{Bmatrix}=\begin{bmatrix}\mathbf{A}_{mm} & \mathbf{0} & \mathbf{B}_{mb} & \mathbf{C}_{md}\\ \mathbf{0} & \mathbf{D}_{ss} & \mathbf{0} & \mathbf{0}\\ \mathbf{B}_{bm} & \mathbf{0} & \mathbf{E}_{bb} & \mathbf{F}_{bd}\\ \mathbf{C}_{dm} & \mathbf{0} & \mathbf{F}_{db} & \mathbf{H}_{dd}\end{bmatrix}\begin{Bmatrix}\boldsymbol{\varepsilon}_m\\ \boldsymbol{\varepsilon}_s\\ \boldsymbol{\varepsilon}_b\\ \boldsymbol{\varepsilon}_d\end{Bmatrix},\ \mathbf{s}=\mathbf{C}^e\boldsymbol{\varepsilon}\,. \tag{12}$$

3.3 TTO formulation

Let (*c*) stands for ceramic and (*m*) for metal constituent. The shell section is assumed as ceramic rich on the top surface $(+h^+)$ and metal rich on the bottom surface $(-h^+)$. The power law

$$V_{\mathrm{c}}=\left(\frac{z}{h}+\frac{1}{2}\right)^n,\quad V_{\mathrm{m}}=1-V_{\mathrm{c}},\quad n\geq 0 \tag{13}$$

describes the distribution of material constituents in the thickness direction *z*. Here n denotes the power-law exponent. Material constituents could be distributed along thickness according to various laws, detailed description and their influence on free vibration of FGM shells is collected in [29].

In the assumed TTO model, see e.g. [2,5,15], materials' mixture is treated as elastoplastic with isotropic linear hardening, with properties described by the following relations

$$E(z)=\left(\frac{q+E_c}{q+E_m}E_mV_m+E_cV_c\right)\Bigg/\left(\frac{q+E_c}{q+E_m}V_m+V_c\right), \tag{14}$$

$$\nu(z)=\nu_cV_c+\nu_mV_m,\ G(z)=\frac{E(z)}{2\left(1+\nu(z)\right)},\ \sigma_Y^0(z)=\sigma_{Ym}^0\left(\frac{q+E_m}{q+E_c}\frac{E_c}{E_m}V_c+V_m\right) \tag{15}$$

$$H(z)=\left(\frac{q+E_c}{q+H_m}H_mV_m+E_cV_c\right)\Bigg/\left(\frac{q+E_c}{q+H_m}V_m+V_c\right). \tag{16}$$

In the above equations $E(z)$ is the effective Young modulus, $\nu(z)$ is the effective Poisson's ratio, $G(z)$ is the shear modulus, q denotes the so-called [5] ratio of stress to strain transfer and $H(z)$ is the multilinear hardening modulus. Cosserat parameters in mixture are defined as follows:

$$l(z)=l_cV_c+l_mV_m,\qquad \kappa(z)=G(z)\frac{N^2}{1-N^2}. \tag{17}$$

3.4 Yield function for TTO Cosserat shell

Within the framework of J_2 plasticity for Cosserat material ([64]) we assume yield function f in the form

$$f=\sqrt{3J_2}-\sigma_Y,\qquad J_2=a_1s_{ij}s_{ij}+a_2s_{ij}s_{ji}+a_3m_{ij}m_{ij}/l^2,\quad s_{ij}=\sigma_{ij}-\tfrac{1}{3}\delta_{ij}\sigma_{kk}. \tag{18}$$

In (18) m_{ij} are the components of the Cosserat couple tensor, cf. [65]. The effective plastic strain is defined as

$$\dot{\bar{\varepsilon}}^{\mathrm{p}}=\left[b_1\dot{e}_{ij}^p\dot{e}_{ij}^p+b_2\dot{e}_{ij}^p\dot{e}_{ji}^p+b_3\dot{\kappa}_{ij}^p\dot{\kappa}_{ij}^pl^2\right]^{1/2},\quad \dot{e}_{ij}=\dot{\varepsilon}_{ij}-\tfrac{1}{3}\delta_{ij}\dot{\varepsilon}_{kk} \tag{19}$$

where the dot denotes the rates of: the deviatoric strain $\dot{e}_{ij}$ and of the 3D Cosserat micro-curvatures $\dot{\kappa}_{ij}^p$. In calculations we assume that constants a_i, b_i, $i=1,2,3$ take on the following values: $a_1=\frac{1}{4}$, $a_2=\frac{1}{4}$, $a_3=\frac{1}{2}$, $b_1=\frac{1}{3}$, $b_2=\frac{1}{3}$, $b_3=\frac{2}{3}$ but other options are also possible, see e.g.

[64]. Thus, assuming also plane stress in each layer of the FGM shell, we obtain from (18) and (19)

$$J_2 = \frac{1}{3}\left(\sigma_{11}^2 + \sigma_{22}^2 - \sigma_{11}\sigma_{22} + \frac{3}{4}\left(\sigma_{12}^2 + \sigma_{21}^2\right) + \frac{3}{2}\sigma_{12}\sigma_{21} + \frac{3}{2l^2}\left(m_{13}^2 + m_{23}^2\right)\right) \tag{20}$$

$$\dot{\bar{\varepsilon}}^{\mathrm{p}} = \left[\frac{2}{3}\left((\dot{e}_{11}^p)^2 + (\dot{e}_{22}^p)^2\right) + \frac{1}{3}(\dot{e}_{12}^p)^2 + \frac{2}{3}\dot{e}_{12}\dot{e}_{21}^p + \frac{1}{3}(\dot{e}_{21}^p)^2 + \frac{2}{3}\left((\dot{\kappa}_{13}^p)^2 + (\dot{\kappa}_{23}^p)^2\right)\right]^{1/2} \tag{21}$$

Classical plasticity formulae [56] is used with for associated flow rule and isotropic linear hardening

$$\dot{\boldsymbol{\varepsilon}}^{\mathrm{p}} = \dot{\gamma}\frac{\partial f}{\partial \boldsymbol{\sigma}}, \qquad \sigma_Y = \sigma_Y^0 + H\gamma\,. \tag{22}$$

Equations of plasticity are integrated using the closest point projection algorithm, e.g. [56], [66] [67] which in the context of the present shell theory has been already discussed thoroughly in [55], therefore the details are omitted here.

4 Results

All calculations presented in this section are based on the own FEM code CAM [52], written in Fortran. The used finite elements (CAMe16) are 16-node elements with full 4×4 Gauss-Legendre integration in the shell reference surface. Through the thickness integration of the constitutive relation is carried out using Gauss-Legendre or Gauss-Lobatto quadrature. Shear correction factor $\alpha_s = 5/6$ is used in present calculations. In each calculation, middle reference surface approach is applied [1] which means that integration in (9)-(10) runs from $-h^- = -h/2$ to $+h^+ = h/2$, where h denotes shell thickness. All quantities are given in unit system N, mm, MPa.

4.1 Rectangular plate under in-plane compression (I type)

FGM rectangular plate, compressed in one direction, is taken into consideration. The dimensions, material data and reference results are obtained from [43]. Geometry and FEM

discretization is shown in Fig. 1. Plate thickness is constant and equal to $h = 3.175$. Discretization makes use of the symmetry of: geometry, loading and deformation. Material parameters are: $n \in \{0,\ 0.5,\ 1.0,\ 2.0,\ 5.0,\ \infty\}$, $E_c = 340000$, $v_c = 0.25$, $l_c = 0.0001$, $E_m = 206200$, $v_m = 0.3$, $l_m = 0.0001$, $H_m = 0$, $\sigma_{Ym}^0 = 250$, $q = 4500$, $\kappa = G$.

At first, comparison of present results and those obtained from [43] is presented. Reference solution was obtained by FEM analysis. Material parameters variation with respect to thickness is defined by equations (14)-(16) which yields smooth distribution from pure metal to pure ceramic layer. Here, following concept presented in [43] an initial geometrical, zero-stress imperfection is introduced. Initial displacement of middle point is assumed as $w_{impf} = b/1000$, with imperfection shape provided by linear static solution for plate deflection.

The obtained results are compared to reference solution [43]. Integration in the direction of thickness is performed using 7-point Gauss-Legendre quadrature. Various rectangular plates are analyzed which differ in assumed b/h and a/b ratios. This gives a spectrum of plates from nearly square with width $b = 40h$ to rectangular $b = 80h$ (see table 1).

Results will be presented as equilibrium curves in the following coordinates $(\varepsilon/\varepsilon_Y, S/S_Y)$, where:

- $\varepsilon = \frac{2u_A}{a}$ is relative shortening of plate;
- $\varepsilon_Y = \frac{\sigma_{Ym}}{E_m}$ is axial strain at which metallic plate starts yielding;
- $S = \frac{P_x}{b \cdot h}$ is average stress, where P_x is total reaction collected form edge $x = 0$;
- $S_Y = \sigma_{Ym}$ is yielding stress for metallic constituent.

The computations are performed for plates with aspect ratios collected in table 1 and following values of power law exponent $n \in \{0,\ 0.5,\ 1.0,\ 2.0,\ 5.0,\ \infty\}$. Limit values of parameter *n* give homogenous perfectly plastic metallic plate ($n = \infty$) or elastic ceramic plate ($n = 0$).

Graphs presented in the Fig. 2-Fig. 7, show the stress ratio S / S_Y with respect to $\varepsilon / \varepsilon_Y$ and displacement w_B of center point B. The authors' curves are compared to reference solution, only results for variant D weren't provided in [43]. It is worth to notice that for long plates (variants D-F) in some analyzes, initial deformation do not conform with the failure mode which leads to turning of the curves back to negative direction of w_B displacement. The present results are in good agreement with reference solution for variant A, B and C (short plates). For long spans (variants E, F) larger differences are visible, especially in equilibrium paths after limit load point is reached. Additionally, contour plots of displacement *w* at the end of analysis for variant F are shown in Fig. 8.

As an additional study, convergence analysis for different rules of through-the-thickness integration is conducted. The following methods are compared: Gauss-Legendre quadrature, Gauss-Lobatto quadrature and thickness division into equal layers (single integration point at the center of each layer). The influence of number of integration points on the limit load is investigated. Compressed plate with dimensions $b/t = 40$, $a/b = 2.625$ and power-law exponent $n = 2.0$ is analyzed. Results collected in Fig. 9, Fig. 10 and Fig. 11 show that in every case the limit loads converge however in different manner. When Gauss-Lobatto quadrature is used, convergence "from top" is observed, as the integration point is placed exactly on purely ceramic elastic layer in every simulation. As the value of weight assigned to this points becomes smaller, the limit load reduces. In Gauss-Legendre quadrature and equal thickness layers calculations, integration point closest to ceramic outer surface is assumed to be elasto-plastic with relatively high hardening modulus. Consequently, latter two methods of through-the-thickness integration gives convergence "from bottom". The algorithm used to integrate elastoplastic material law implemented in author's FEM code was not able to obtain convergence in Gauss-Legendre quadratures with 17, 19 and 21 integration points in those limit points, due to relatively high value of tangent hardening modulus in highest fraction of ceramic constituent.

It can be argued that usage of Gauss quadratures requires less integration points in comparison to equal-layer method to obtain comparable results. On the other hand, differences are relatively small, thus the equal thickness layers method is acceptable where application of classical quadratures for FGM shell is not possible (like in commercial codes).

4.2 Rectangular plate under in-plane compression (II type)

We analyze the compressed plate proposed in [42]. The problem is similar to previous one (with different geometry and material data) yet here the reference solutions are obtained by analytical derivations. Geometrical dimensions are (according to notation in Fig. 1) $a=200$, $b=100$, $b/t\in\{20,\ 25,\ 30,\ 40,\ 50,\ 60,\ 80,\ 100\}$. Perfect flat initial geometry is assumed in analysis. Material data is defined as: $n\in\{0.2,\ 5.0\}$, $E_c=375000$, $\nu_c=0.14$, $l_c=0.005$, $E_m=107000$, $\nu_m=0.34$, $l_m=0.005$, $H_m=4600$, $\sigma_{Ym}^0=450$, $q=4500$, $\kappa=G$.

Equilibrium paths obtained in geometrically and materially nonlinear FEM analysis are presented in Fig. 12 and Fig. 13. Our nonlinear curves are compared to analytically obtained critical loads from paper [42]. In this case it could be assumed that buckling occurs when central point displacement w_B become non-zero. Results show good agreement between reference and present values of buckling load. Contour plots of displacement *w*, placed on right sides of Fig. 12 and Fig. 13, reveal the same final deformation shape in every case, namely 3 half waves along compression direction and 1 half wave in perpendicular direction.

Additionally, the present investigations give further insight into behavior of the compressed plate. Namely, stable postbuckling increase of strength of whole structure for $n=0.2$ and clear limit load points obtained in $n=5.0$ cases can be noticed. For thin plates ($b/t\in\{60,\ 80,\ 100\}$), buckling occurs prior to the first yielding while for thicker plates buckling is in partially yielded structure.

4.3 Elastoplastic bucking of axially loaded cylindrical shell

Cylindrical shells are often used in engineering practice. Their statics and dynamics has been extensively studied in the literature and it always is a challenge. Theoretical foundations may be traced back to the book by [68]. Static numerical analysis of such shells requires special techniques to trace the equilibrium path, such as for instance arc-length control or displacement control, see for instance Ramm or Crisfield in [69]. Another approach is to employ dynamic analysis e.g. [70,71][72]. However, such analysis is also demanding and theoretical results are therefore always important. The present example is taken from [5] and is used to validate the present formulation. Axially loaded cylindrical shell was considered there both analytically and numerically. The material parameters are: $n=1.0$, $E_c=3.75\cdot10^5$, $E_m=1.07\cdot10^5$, $\nu_c=0.14$, $\nu_m=0.34$, $H_m=14000$, $\sigma_{Ym}^0=450$, $q=4500$, $\kappa=G$, characteristic length of metal and ceramic are equal $l_m=l_c=0.01h$. The inner surface is ceramic-rich. Proportional load is assumed as $P(\lambda)=\lambda P_{ref}$, $P_{ref}=1000$. The geometry of the shell is presented in Fig. 14. The number of CAMe16 elements along the height is 52 while in the circumferential direction equals to 64.

The displacement control was used to trace the equilibrium path with the control displacement v of the top of the shell. The load is understood as the sum of reaction at upper edge. The present results are compared with reference solution from [5] and with own Abaqus commercial code calculations in Fig. 15 and Table 2. In Abaqus, 31715 nodes, 31400 elements S4R and 20 or 7 layers (with single integration point in the middle of each layer in thickness integration) were used in simulation. It can be noticed that all the results are in good agreement.

In addition, in Fig. 16, we present load-deformation path for thickness $h=0.2$. Abaqus results were obtained with different types of finite elements and number of composite layers whereas CAM results with 7 integration points (Gauss-Legendre rule) in the thickness direction. It can be observed that once the limit point is reached there appear some discrepancies among

the results which are attributed to different element formulations and depend on the approximation of the material structure in the thickness direction.

Moreover, to investigate the jump observed on CAMe16 equilibrium path we analyze two deformation states indicated in Fig. 16 as point A and point A'. The results are shown in Fig. 17 and in Fig. 18. It is visible that the observed jump is attributed to the presence of new deformation wave localized close to the bottom and top edge. The contour plot of effective plastic strains is presented in Fig. 18 for the first and last through-the-thickness integration point. In Gauss-Legendre quadrature those points are located closely to inner and outer surface but not directly on them.

Shell deformation at limit load point is compared with deformation at the end of analysis (final point of curves in Fig. 15) for different values of shell thickness in Fig. 19. The plots show that when $h \in \{0.15,\ 0.2,\ 0.3,\ 0.4\}$, the final deformation is asymmetric, however deformation is still axially symmetric. Obviously, waves forms along the ruling of cylinder, but those are far from being regular sine-type function like assumed in analytical solution, see [5]. These results show indeed that present example is very demanding test, because of complex deformation at final configuration.

4.4 Box section column under axial load

In this example we analyze the shell with orthogonal intersections. Nonlinear response and load capacity of axially loaded box section column is studied. The geometry and boundary conditions are shown in Fig. 20. The material parameters are: $E_c = 3.75 \cdot 10^5$, $E_m = 1.07 \cdot 10^5$, $\nu_c = 0.14$, $\nu_m = 0.34$, $H_m = 4600$, $\sigma_Y = 450$, $q = 4500$, $\kappa = G$, $l_m = l_c = 0.0002$. Dimensions of the structure are assumed as: width of the cross section $a = 100$, depth $b = 50$, height $L = 200$, uniform shell thickness $h = 2$. The inner surface is metal-rich. The displacement control was used to trace the equilibrium path with the control displacement v of the top edge of the column. The study of the influence of the power-law exponent n on the results is performed. The equilibrium paths with respect to the displacements v_A and w_B for variable n

are shown in Fig. 21. With the decrease of n the limit points become less pronounced, however the curves exhibit plateau-like shape. For $n = 5.0$ and $n = \infty$ it was possible to find the maximum of the curve, the respective values of limit loads are given in Fig. 21. It is also worth noticing, that in case $n = \infty$ displacement w_B changes sign, namely at the beginning of analysis point B is moving outwards the box section, however at a load level 1.041×10^5 direction of movement rapidly changes and finally point B is placed inside section, like for other values of *n*.

In Fig. 22 typical deformation is presented, with 3 half-waves along axis of the box. Contours of reduced, Huber-Mises-Hencky type stresses (20) (purely ceramic material) or equivalent plastic strain (mixed material) are shown in inner most, metallic layer.

5 Conclusions

We have successfully formulated elastoplastic constitutive relation for FGM shells with Cosserat-type kinematics with associated FEM implementation. The formulation is capable of dealing with unlimited translations and rotations. In particular, due to the natural presence of the so-called drilling rotation at the element node, the presented formulation is particularly well-suited for the simulations where orthogonal shell branches appear. The obtained results are in good correspondence with analytical ([5,42]) and numerical reference solution ([43] and own Abaqus calculations). The presented results support the following conclusions:

- Numerical stability analysis of cylindrical shells in the post-limit range is particularly demanding, the results may depend on the FEM formulation and discretization. Thus, analytical or experimental results are indispensable to validate the formulation.
- Application of different quadrature rules in the thickness direction provides lower or upper bound of the result.
- Nonlinear FEM analysis gave insight in postbuckling deformation of compressed structures. In case of cylindrical geometry, deformation is more complicated than described by the product of the sine and cosine functions, like in analytical solutions [5,42].

- In papers by Huang and co-workers [5,42] critical loads were calculated. The values of our critical loads are in good agreement with reference values in case of compressed plate, but for cylindrical shell these meet with limit loads, even though buckling is not observed at this point (deformation gradually forms since start of loading, without noticeable change of its shape). Sudden change of shape is noticed after load passes limit load point.

Acknowledgements

The research reported in this paper was supported by the National Science Centre, Poland with the grant UMO-2015/17/B/ST8/02190. Parallel solver for CAM elements is developed on the basis of HSL, a collection of Fortran codes for large-scale scientific computation. http://www.hsl.rl.ac.uk. Abaqus calculations were carried out at the Academic Computer Centre in Gdańsk.

References

[1] Burzyński S, Chróścielewski J, Daszkiewicz K, Witkowski W. Geometrically nonlinear FEM analysis of FGM shells based on neutral physical surface approach in 6-parameter shell theory. Compos Part B Eng 2016;107:203–13. doi:10.1016/j.compositesb.2016.09.015.

[2] Tamura I, Tomota Y, Ozawa M. Strength and Ductility of Iron-Nickel-Carbon Alloys Composed of Austenite and Martensite with Various Strength. 3rd Int. Conf. Strength Met. Alloy., Cambridge: Institute of Metal and Iron; 1973, p. 611–5.

[3] Shen M, Bever MB. Gradients in polymeric materials. J Mater Sci 1972;7:741–6. doi:10.1007/BF00549902.

[4] Koizumi M. FGM activities in Japan. Compos Part B Eng 1997;28:1–4. doi:10.1016/S1359-8368(96)00016-9.

[5] Huang H, Han Q. Elastoplastic buckling of axially loaded functionally graded material cylindrical shells. Compos Struct 2014;117:135–42. doi:10.1016/j.compstruct.2014.06.018.

[6] Jin ZH, Paulino GH, Dodds RH. Cohesive fracture modeling of elastic-plastic crack growth in functionally graded materials. Eng Fract Mech 2003;70:1885–912. doi:10.1016/S0013-7944(03)00130-9.

[7] Shabana YM, Noda N. Thermo-elasto-plastic stresses in functionally graded materials subjected to thermal loading taking residual stresses of the fabrication process into consideration. Compos Part B Eng 2001;32:111–21. doi:10.1016/S1359-8368(00)00049-4.

[8] Amirpour M, Das R, Bickerton S. An elasto-plastic damage model for functionally graded plates with in-plane material properties variation: Material model and numerical implementation. Compos Struct 2017;163:331–41. doi:10.1016/j.compstruct.2016.12.020.

[9] Baghani M, Fereidoonnezhad B. Limit analysis of FGM circular plates subjected to arbitrary rotational symmetric loads using von-Mises yield criterion. Acta Mech 2013;224:1601–8. doi:10.1007/s00707-013-0828-z.

[10] Ghannadpour SAM, Alinia MM. Large deflection behavior of functionally graded plates under pressure loads. Compos Struct 2006;75:67–71. doi:10.1016/j.compstruct.2006.04.004.

[11] Sharma K, Kumar D. Elastoplastic analysis of FGM plate with a central cutout of various shapes under thermomechanical loading. J Therm Stress 2017;40:1417–41. doi:10.1080/01495739.2017.1323566.

[12] Akis T. Elastoplastic analysis of functionally graded spherical pressure vessels. Comput Mater Sci 2009;46:545–54. doi:10.1016/j.commatsci.2009.04.017.

[13] Arciniega RA, Reddy JN. Large deformation analysis of functionally graded shells. Int J Solids Struct 2007;44:2036–52. doi:10.1016/j.ijsolstr.2006.08.035.

[14] Han SC, Lee WH, Park WT. Non-linear analysis of laminated composite and sigmoid functionally graded anisotropic structures using a higher-order shear deformable natural Lagrangian shell element. Compos Struct 2009;89:8–19. doi:10.1016/j.compstruct.2008.08.006.

[15] Zhang Y, Huang H, Han Q. Buckling of elastoplastic functionally graded cylindrical shells under combined compression and pressure. Compos Part B Eng 2015;69:120–6. doi:10.1016/j.compositesb.2014.09.024.

[16] Zhang DG, Zhou HM. Mechanical and thermal post-buckling analysis of FGM rectangular plates with various supported boundaries resting on nonlinear elastic foundations. Thin-Walled Struct 2015;89:142–51. doi:10.1016/j.tws.2014.12.021.

[17] Taczała M, Buczkowski R, Kleiber M. Nonlinear buckling and post-buckling response of stiffened FGM plates in thermal environments. Compos Part B Eng 2017;109:238–47. doi:10.1016/j.compositesb.2016.09.023.

[18] Huang H, Chen B, Han Q. Investigation on buckling behaviors of elastoplastic functionally graded cylindrical shells subjected to torsional loads. Compos Struct 2014;118:234–40. doi:10.1016/j.compstruct.2014.07.025.

[19] Woo J, Meguid SA. Nonlinear analysis of functionally graded plates and shallow shells. Int J Solids Struct 2001;38:7409–21. doi:10.1016/S0020-7683(01)00048-8.

[20] Fazzolari FA. Generalized exponential, polynomial and trigonometric theories for vibration and stability analysis of porous FG sandwich beams resting on elastic foundations. Compos Part B Eng 2018;136:254–71. doi:10.1016/j.compositesb.2017.10.022.

[21] Nguyen TT, Lee J. Optimal design of thin-walled functionally graded beams for buckling problems. Compos Struct 2017;179:459–67. doi:10.1016/j.compstruct.2017.07.024.

[22] Rizov V. Delamination fracture in a functionally graded multilayered beam with material nonlinearity. Arch Appl Mech 2017;87:1037–48. doi:10.1142/S0219455418500517.

[23] Swaminathan K, Naveenkumar DT, Zenkour AM, Carrera E. Stress , vibration and buckling analyses of FGM plates — A state- of-the-art review. Compos Struct 2015;120:10–31. doi:10.1016/j.compstruct.2014.09.070.

[24] Jha DK, Kant T, Singh RK. A critical review of recent research on functionally graded plates. Compos Struct 2013;96:833–49. doi:10.1016/j.compstruct.2012.09.001.

[25] Birman V, Byrd LW. Modeling and analysis of functionally graded materials and structures. ASME Appl Mech Rev 2007;60:195–216. doi:10.1115/1.2777164.

[26] Fazzolari FA. Reissner's Mixed Variational Theorem and variable kinematics in the modelling of laminated composite and FGM doubly-curved shells. Compos Part B Eng 2016;89:408–23. doi:10.1016/j.compositesb.2015.11.031.

[27] Tornabene F, Fantuzzi N, Bacciocchi M, Reddy J. An Equivalent Layer-Wise Approach for the Free Vibration Analysis of Thick and Thin Laminated and Sandwich Shells. Appl Sci 2016;7:17. doi:10.3390/app7010017.

[28] Tornabene F, Brischetto S, Fantuzzi N, Bacciocchi M. Boundary conditions in 2D numerical and 3D exact models for cylindrical bending analysis of functionally graded structures. Shock Vib 2016;2016. doi:10.1155/2016/2373862.

[29] Tornabene F, Fantuzzi N, Bacciocchi M. Free vibrations of free-form doubly-curved shells made of functionally graded materials using higher-order equivalent single layer theories. Compos Part

B Eng 2014;67:490–509. doi:10.1016/j.compositesb.2014.08.012.

[30] Williamson RL, Rabin BH, Drake JT. Finite element analysis of thermal residual stresses at graded ceramic-metal interfaces. Part I. Model description and geometrical effects. J Appl Phys 1993;74:1310–20. doi:10.1063/1.354910.

[31] Drake JT, Williamson RL, Rabin BH. Finite element analysis of thermal residual stresses at graded ceramic-metal interfaces. Part II. Interface optimization for residual stress reduction. J Appl Phys 1993;74:1321–6. doi:10.1063/1.354911.

[32] Aboudi J, Pindera M-J, Arnold SM. Thermo-inelastic response of functionally graded composites. Int J Solids Struct 1995;32:1675–710. doi:10.1016/0020-7683(94)00201-7.

[33] Weissenbek E, Pettermann HE, Suresh S. Elasto-plastic deformation of compositionally graded metal-ceramic composites. Acta Mater 1997;45:3401–17. doi:10.1016/S1359-6454(96)00403-X.

[34] Nakamura T, Wang T, Sampath S. Determination of Properties of Graded Materials. Acta Metall 2000;48:4293–306.

[35] Gu Y, Nakamura T, Prchlik L, Sampath S, Wallace J. Micro-indentation and inverse analysis to characterize elastic–plastic graded materials. Mater Sci Eng A 2003;345:223–33. doi:10.1016/S0921-5093(02)00462-8.

[36] Gunes R, Aydin M, Apalak MK, Reddy JN. The elasto-plastic impact analysis of functionally graded circular plates under low-velocities. Compos Struct 2011;93:860–9. doi:10.1016/j.compstruct.2010.07.008.

[37] Gunes R, Aydin M, Kemal Apalak M, Reddy JN. Experimental and numerical investigations of low velocity impact on functionally graded circular plates. Compos Part B Eng 2014;59:21–32. doi:10.1016/j.compositesb.2013.11.022.

[38] Kalali AT, Hassani B, Hadidi-Moud S. Elastic-plastic analysis of pressure vessels and rotating disks made of functionally graded materials using the isogeometric approach. J Theor Appl Mech 2016:113. doi:10.15632/jtam-pl.54.1.113.

[39] Sharma K, Kumar D. Elastoplastic stability and failure analysis of FGM plate with temperature dependent material properties under thermomechanical loading. Lat Am J Solids Struct 2017;14:1361–86. doi:10.1590/1679-78253747.

[40] Zhang DG, Zhou HM. Mechanical and thermal post-buckling analysis of FGM rectangular plates with various supported boundaries resting on nonlinear elastic foundations. Thin-Walled Struct

2015;89:142–51. doi:10.1016/j.tws.2014.12.021.

[41] Huang H, Zhang Y, Han Q. Inelastic Buckling of FGM Cylindrical Shells Subjected to Combined Axial and Torsional Loads. Int J Struct Stab Dyn 2017;17:1771010. doi:10.1142/S0219455417710109.

[42] Xu G, Huang H, Chen B, Chen F. Buckling and postbuckling of elastoplastic FGM plates under inplane loads. Compos Struct 2017;176:225–33. doi:10.1016/j.compstruct.2017.04.061.

[43] Kleiber M, Taczała M, Buczkowski R. Elasto-Plastic Response of Thick Plates Built in Functionally Graded Material Using the Third Order Plate Theory. Adv. Comput. Plast., vol. 46, 2018, p. 185–99. doi:10.1007/978-3-319-60885-3.

[44] Amirpour M, Das R, Saavedra Flores EI. Analytical solutions for elastic deformation of functionally graded thick plates with in-plane stiffness variation using higher order shear deformation theory. Compos Part B Eng 2016;94:109–21. doi:10.1016/j.compositesb.2016.03.040.

[45] Reissner E. Linear and nonlinear theory of shells. In: Fung YC, Sechler EE, editors. Thin Shell Struct., Englewood Cliffs: Prentice-Hall; 1974, p. 29–44.

[46] Libai A, Simmonds JG. The Nonlinear Theory of Elastic Shells. Cambridge: Cambridge University Press; 1998.

[47] Chróścielewski J, Makowski J, Pietraszkiewicz W. Statyka i Dynamika Powłok Wielopłatowych. Nieliniowa teoria i metoda elementów skończonych. Warszawa: Wydawnictwo IPPT PAN; 2004.

[48] Chróścielewski J, Sabik A, Sobczyk B, Witkowski W. Nonlinear FEM 2D failure onset prediction of composite shells based on 6-parameter shell theory. Thin-Walled Struct 2016;105:207–19. doi:10.1016/j.tws.2016.03.024.

[49] Nowacki W. Couple-stresses in the theory of thermoelasticity. In: Parkus H, Sedov LI, editors. Irreversible Asp. Contin. Mech. Transf. Phys. Charact. Mov. fluids. IUTAM Symp. Vienna 1966, Wien: Springer-Verlag; 1968, p. 259–78.

[50] Eringen AC. Microcontinuum Field Theories. I. Foundations and Solids. New York: Springer-Verlag; 1999.

[51] Altenbach J, Altenbach H, Eremeyev VA. On generalized Cosserat-type theories of plates and shells: A short review and bibliography. Arch Appl Mech 2010;80:73–92. doi:10.1007/s00419-009-0365-3.

[52] Chróścielewski J, Makowski J, Stumpf H. Genuinely resultant shell finite elements accounting for geometric and material non-linearity. Int J Numer Methods Eng 1992;35:63–94. doi:10.1002/nme.1620350105.

[53] Chróścielewski J, Kreja I, Sabik A, Witkowski W. Modeling of composite shells in 6-parameter nonlinear theory with drilling degree of freedom. Mech Adv Mater Struct 2011;18:403–19. doi:10.1080/15376494.2010.524972.

[54] Burzyński S, Chróścielewski J, Witkowski W. Geometrically nonlinear FEM analysis of 6-parameter resultant shell theory based on 2-D Cosserat constitutive model. ZAMM - J Appl Math Mech / Zeitschrift Für Angew Math Und Mech 2016;96:191–204. doi:10.1002/zamm.201400092.

[55] Burzyński S, Chroscielewski J, Witkowski W. Elastoplastic law of Cosserat type in shell theory with drilling rotation. Math Mech Solids 2015;20:790–805. doi:10.1177/1081286514554351.

[56] Neto EA de S, Peric D, Owen DRJ. Computational Methods for Plasticity: Theory and Applications. 2009. doi:10.1002/9780470694626.

[57] Daszkiewicz K, Chróścielewski J, Witkowski W. Geometrically Nonlinear Analysis of Functionally Graded Shells Based on 2-D Cosserat Constitutive Model. Eng Trans 2014;62:109–30.

[58] Tornabene F, Fantuzzi N, Bacciocchi M. Mechanical behaviour of composite Cosserat solids in elastic problems with holes and discontinuities. Compos Struct 2017;179:468–81. doi:10.1016/j.compstruct.2017.07.087.

[59] Fantuzzi N, Leonetti L, Trovalusci P, Tornabene F. Some Novel Numerical Applications of Cosserat Continua. Int J Comput Methods 2017;15:1–38. doi:10.1142/S0219876218500548.

[60] Tang H, Sun F, Zhang Y, Dong Y. Elastoplastic axisymmetric Cosserat continua and modelling of strain localization. Comput Geotech 2018;101:159–67. doi:10.1016/j.compgeo.2018.05.004.

[61] Godio M, Stefanou I, Sab K, Sulem J. Multisurface plasticity for Cosserat materials: Plate element implementation and validation. Int J Numer Methods Eng 2016;108:456–84. doi:10.1002/nme.5219.

[62] Nowacki W. Theory of asymmetric elasticity. Oxford: Pergamon Press; 1986.

[63] Jeong J, Ramezani H, Münch I, Neff P. A numerical study for linear isotropic Cosserat elasticity with conformally invariant curvature. ZAMM Zeitschrift Fur Angew Math Und Mech 2009;89:552–69. doi:10.1002/zamm.200800218.

[64] de Borst R. Simulation of strain localization: a reappraisal of the Cosserat continuum. Eng Comput 1991;8:317–32.

[65] Nowacki W. Teoria niesymetrycznej sprężystości. Warszawa: IPPT PAN; 1971.

[66] Simo JC, Hughes TJR. Computational Inelasticity. Springer-Verlag New York, Inc.; 1998.

[67] Belytschko T, Liu N-W, Moran B. Nonlinear Finite Elements for Continua and Structures. John Wiley & Sons, Ltd.; 2003.

[68] Timoshenko S, Gere JM. Theory of elastic stability. 2nd ed. New York: McGraw-Hill; 1961.

[69] Wunderlich W, Stein E, Bathe KJ. Nonlinear Finite Element Analysis in Structural Mechanics. Springer; 1981.

[70] Kołakowski Z. Some aspects of dynamic interactive buckling of composite columns. Thin-Walled Struct 2007;45:866–71. doi:10.1016/j.tws.2007.08.008.

[71] Iwicki P, Tejchman J, Chróścielewski J. Dynamic FE simulations of buckling process in thin-walled cylindrical metal silos. Thin-Walled Struct 2014;84:344–59. doi:10.1016/j.tws.2014.07.011.

[72] Kolakowski Z, Kubiak T. Interactive dynamic buckling of orthotropic thin-walled channels subjected to in-plane pulse loading. Compos Struct 2007;81:222–32. doi:10.1016/j.compstruct.2006.08.012.

Figures' captions

Fig. 1. Compressed plate: geometry, imperfection, load and boundary conditions.

Fig. 2 Compressed plate: equilibrium paths for variant A ($b/t=40$, $a/b=0.875$).

Fig. 3 Compressed plate: equilibrium paths for variant B ($b/t=55$, $a/b=0.875$).

Fig. 4 Compressed plate: equilibrium paths for variant C ($b/t=80$, $a/b=0.875$).

Fig. 5 Compressed plate: equilibrium paths for variant D ($b/t=40$, $a/b=2.625$).

Fig. 6 Compressed plate: equilibrium paths for variant E ($b/t=55$, $a/b=2.625$).

Fig. 7 Compressed plate: equilibrium paths for variant F ($b/t=80$, $a/b=2.625$).

Fig. 8 Compressed plate: final contour plots of displacement *w* for variant F ($b/t=80$, $a/b=2.625$).

Fig. 9 Compressed plate: limit load point convergence study with respect to relative shortening $\varepsilon / \varepsilon_Y$, the influence of number of integration points in thickness direction.

Fig. 10 Compressed plate: limit load point convergence study with respect to center point deflection w_B, the influence of number of integration points.

Fig. 11 Compressed plate: limit load point convergence study with respect to number of integration points.

Fig. 12 Compressed plate: average stress vs. central deflection curves for $n = 0.2$, contour plots of displacement *w* at the end of analysis (right side)

Fig. 13 Compressed plate: average stress vs. central deflection curves for $n = 5.0$, contour plots of displacement *w* at the end of analysis (right side).

Fig. 14. Cylindrical shell under action of axial load, geometry and boundary conditions.

Fig. 15. Cylindrical shell under action of axial load, authors' load-deformation curves, the influence of thickness *h*.

Fig. 16. Cylindrical shell under action of axial load, load-deformation path, $h = 0.2$

Fig. 17. Cylindrical shell under action of axial load, deformation detail and radial displacement before (point A) and after (point A') the jump on equilibrium path.

Fig. 18. Cylindrical shell under action of axial load, effective plastic strain closely to inner and outer surface.

Fig. 19. Deformation of cylindrical shell in radial direction along its ruling (line parallel to *y* axis).

Fig. 20. Axially loaded box section column, geometry and boundary conditions

Fig. 21. Axially loaded box section column, influence of *n* on load-displacement path of v_A

Fig. 22. Axially loaded box section column, deformation shape and contours of H-M-H stress and equivalent plastic strain

Table 1 Dimensions of analyzed variants of compressed plate.

variant	b/h	a/b	h	a	b	w_{impf}	1/4 plate discretization
A	40	0.875	3.175	111.125	127.0	0.127	8x8 CAMe16

B	55	0.875	3.175	152.8	174.625	0.175	8x8 CAMe16
C	80	0.875	3.175	222.25	254	0.254	8x8 CAMe16
D	40	2.625	3.175	333.375	127.0	0.127	24x8 CAMe16
E	55	2.625	3.175	458.4	174.625	0.175	24x8 CAMe16
F	80	2.625	3.175	666.75	254	0.254	24x8 CAMe16

Table 2. Limit loads for axially loaded cylindrical shell, the influence of thickness *h*

	h						
	0.05	0.1	0.15	0.20	0.30	0.40	0.50
analytical Ref [5]	1.854	7.412	14.472	22.757	44.716	75.232	117.459
present formulation CAM	1.862	7.027	14.298	23.538	46.619	72.705	103.530
Abaqus S4R, 20 layers	1.841	7.020	14.309	22.827	46.855	74.482	108.218
Abaqus S4R, 7 layers	1.817	6.848	13.898	22.756	45.188	70.183	102.968

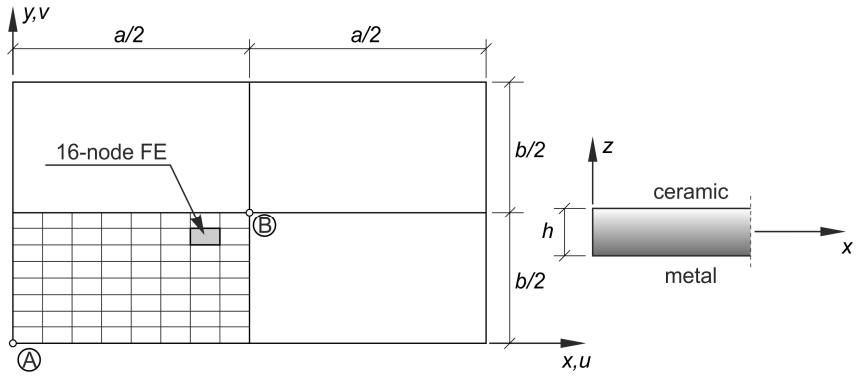

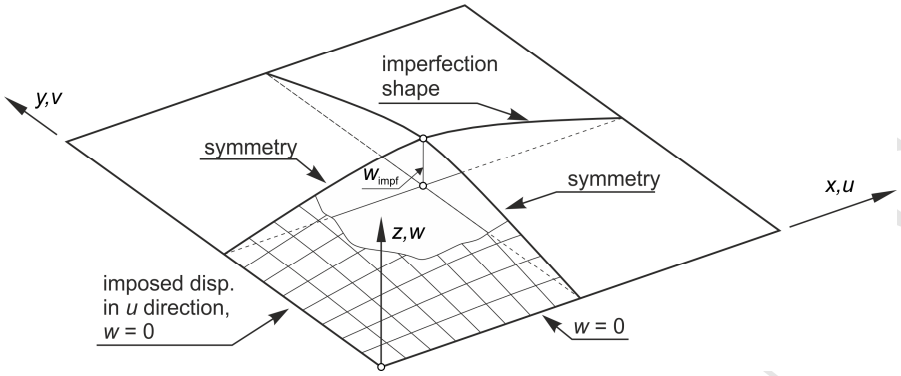

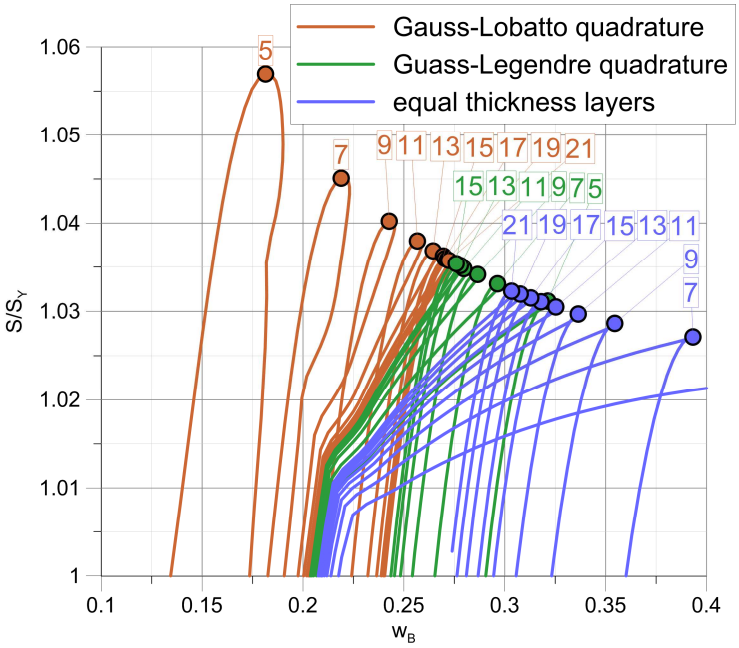

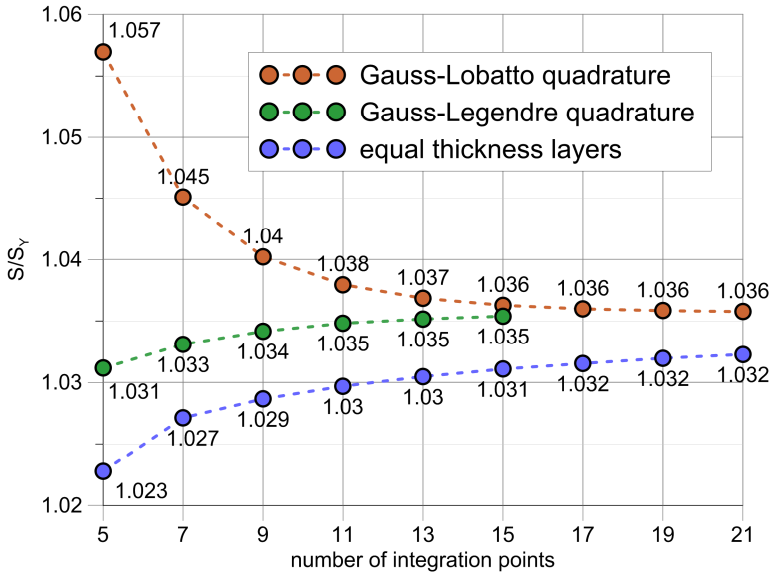

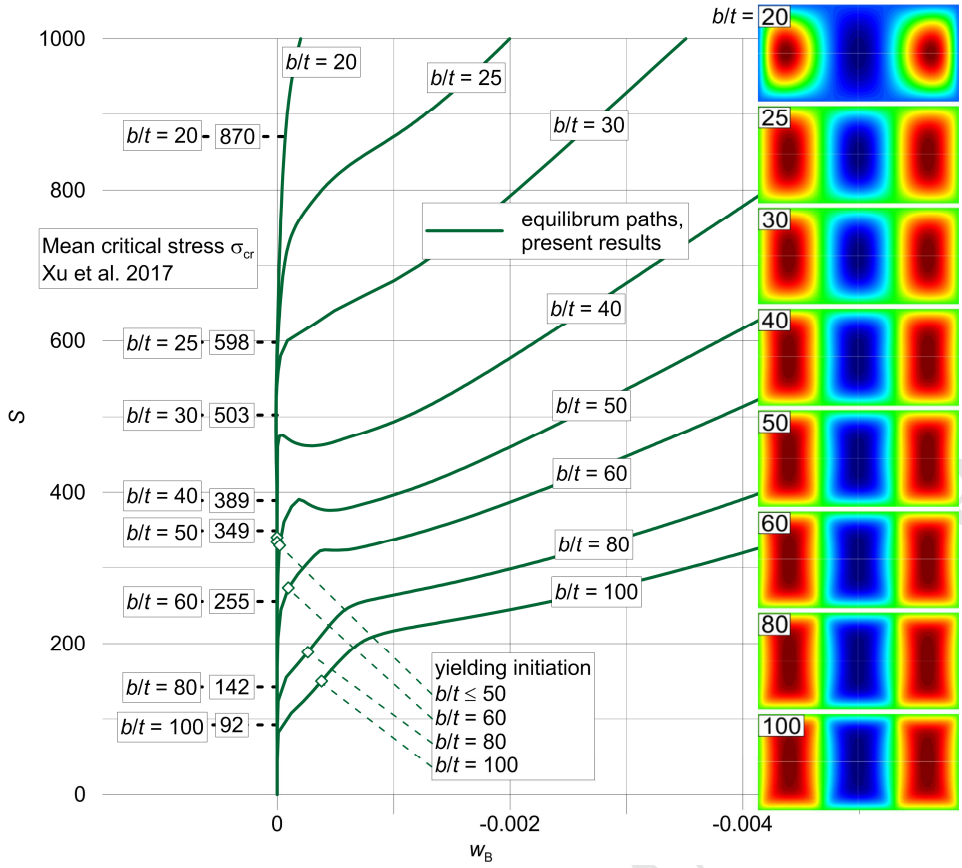

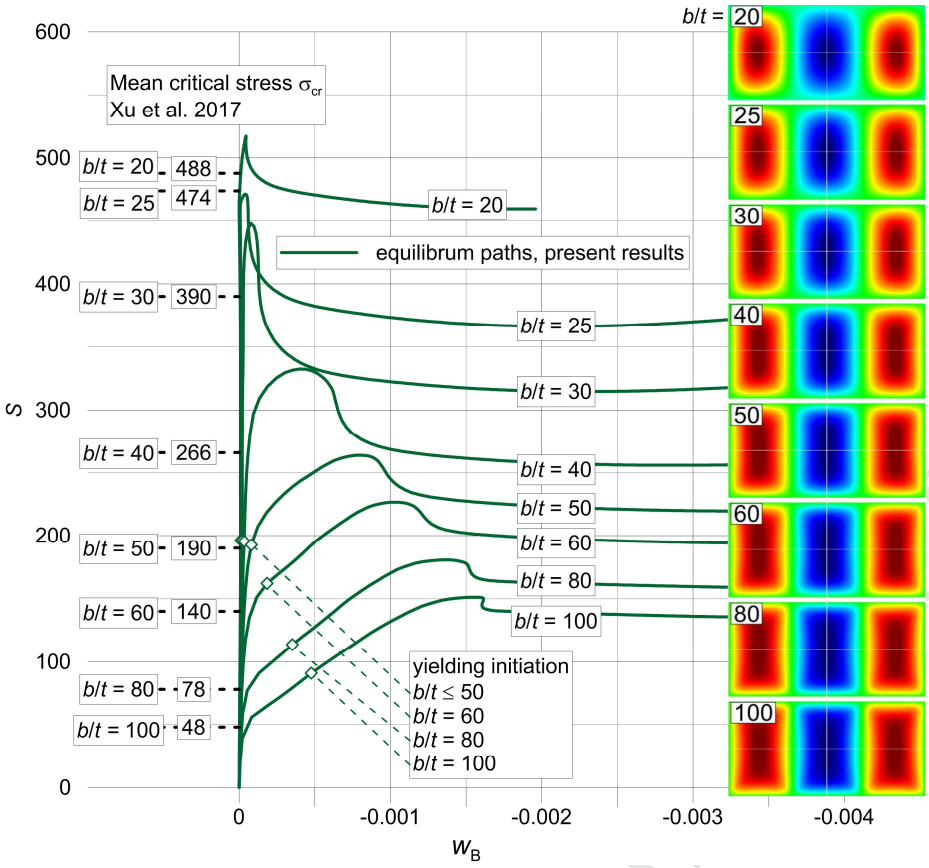

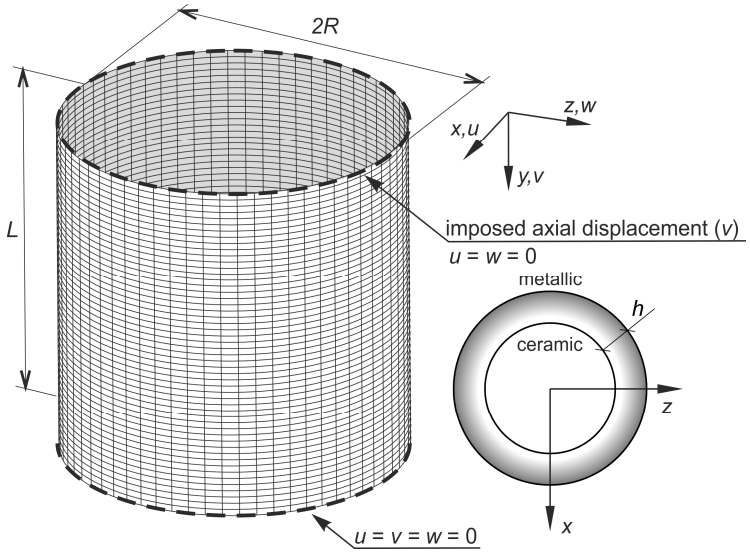

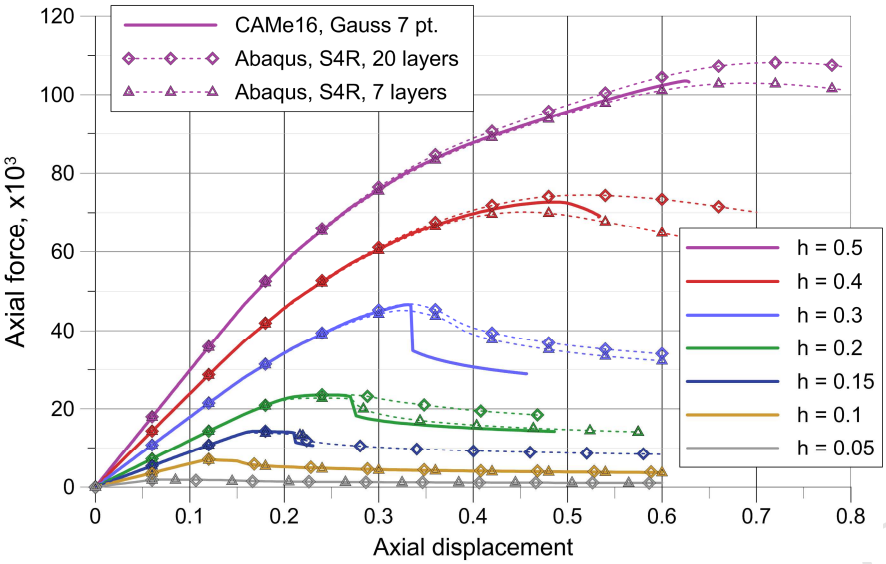

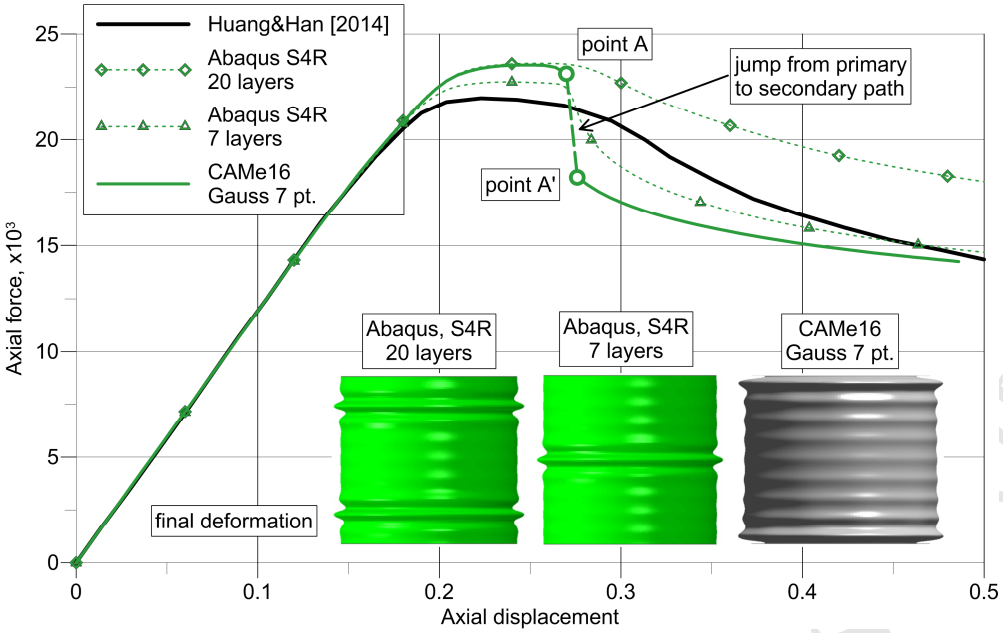

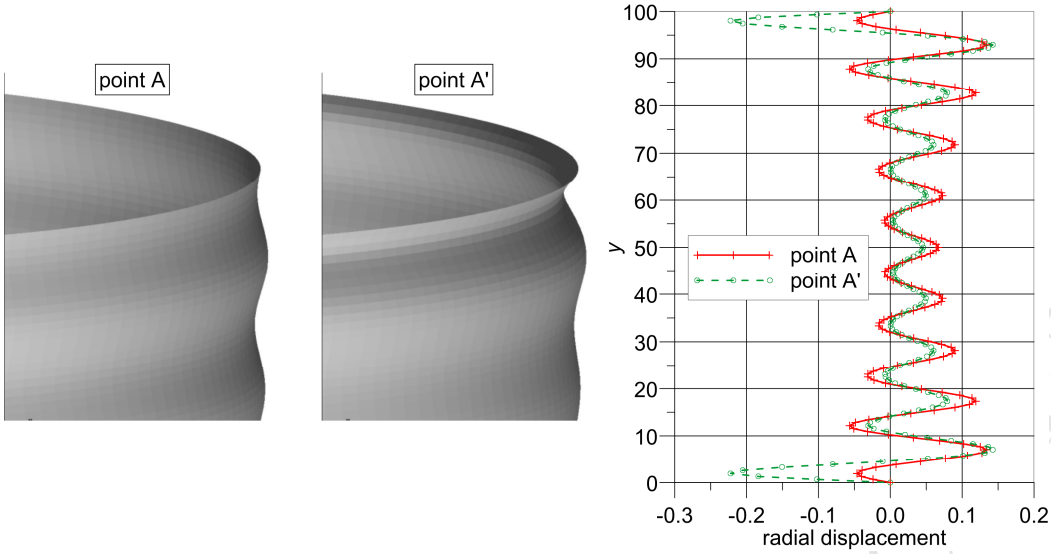

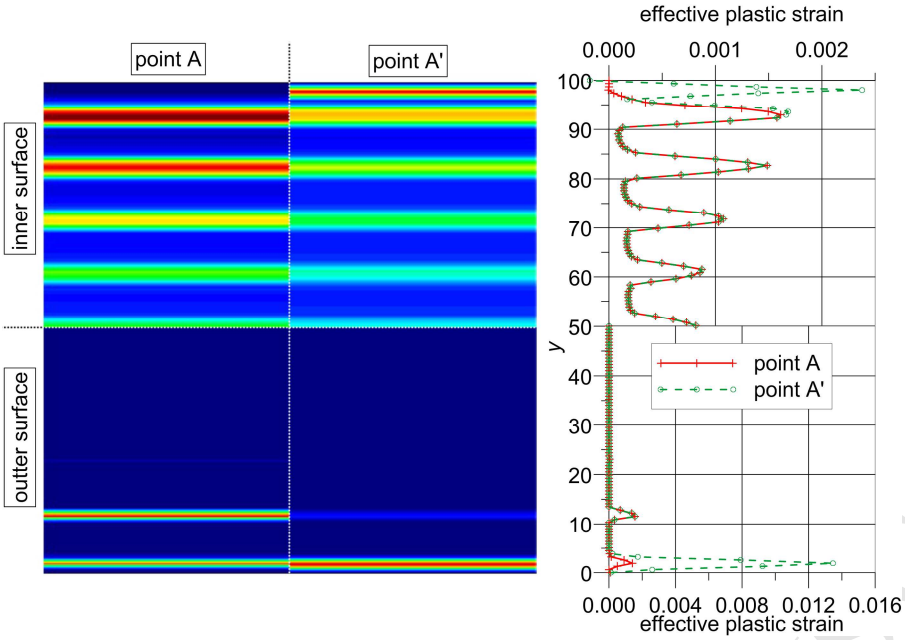

a) h = 0.05

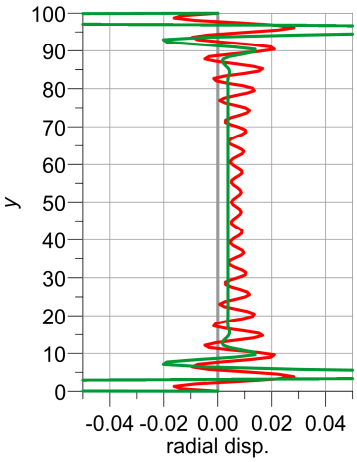

b) h = 0.1

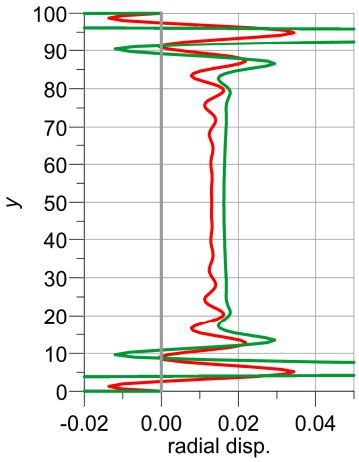

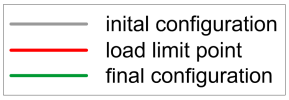

c) h = 0.15

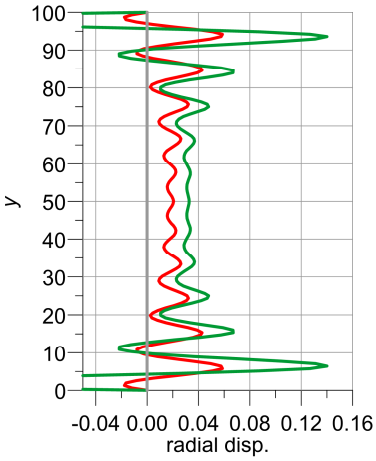

d) h = 0.2

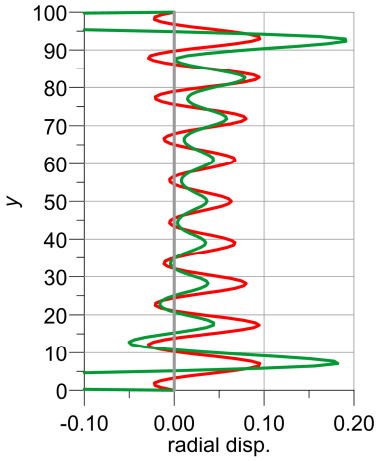

e) h = 0.3

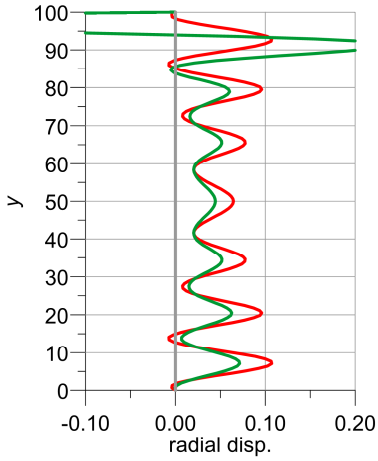

f) h = 0.4

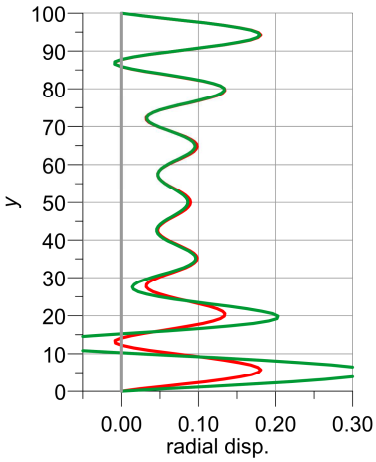

g) h = 0.5

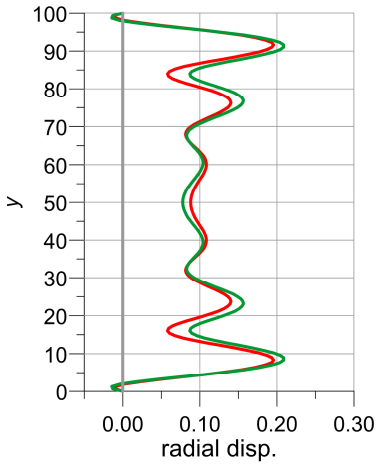

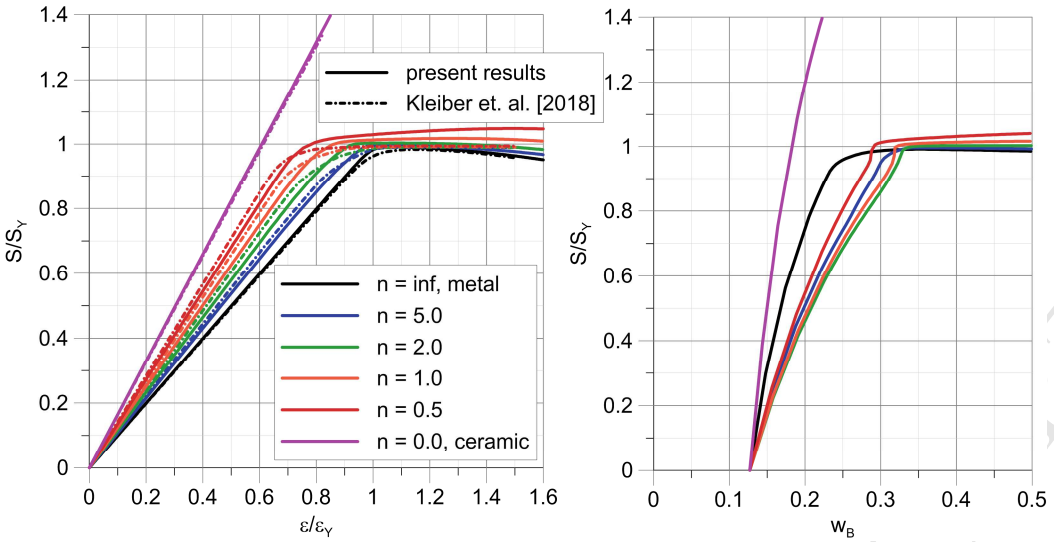

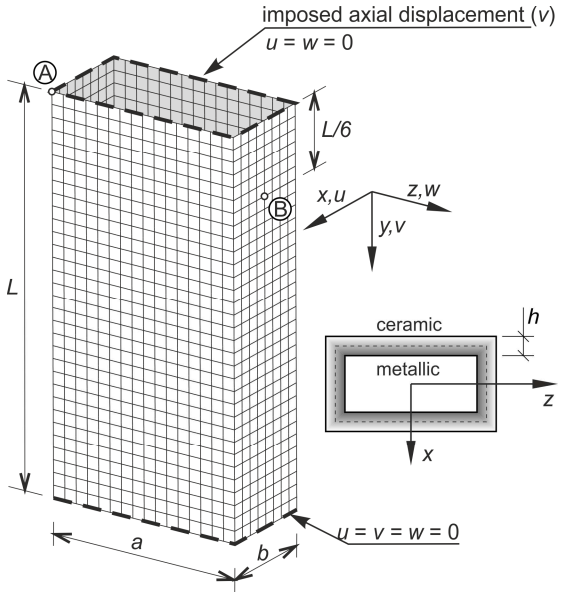

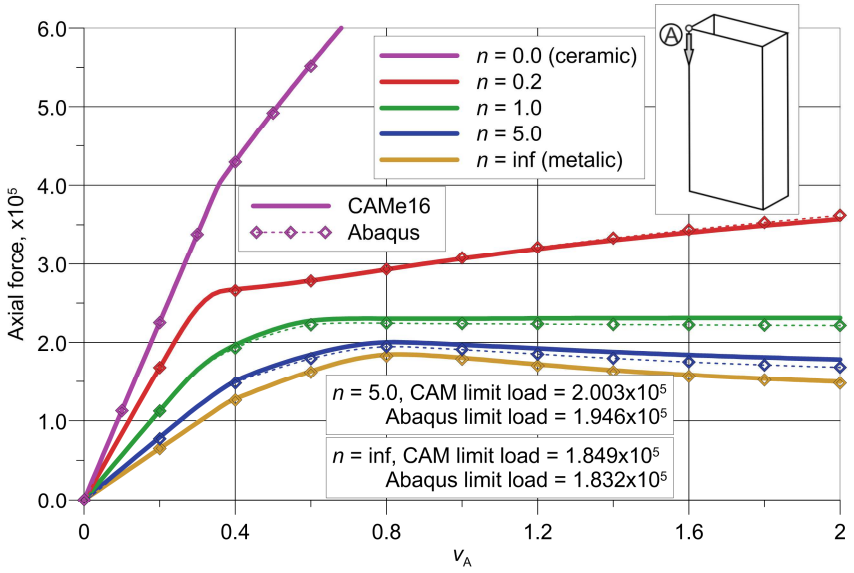

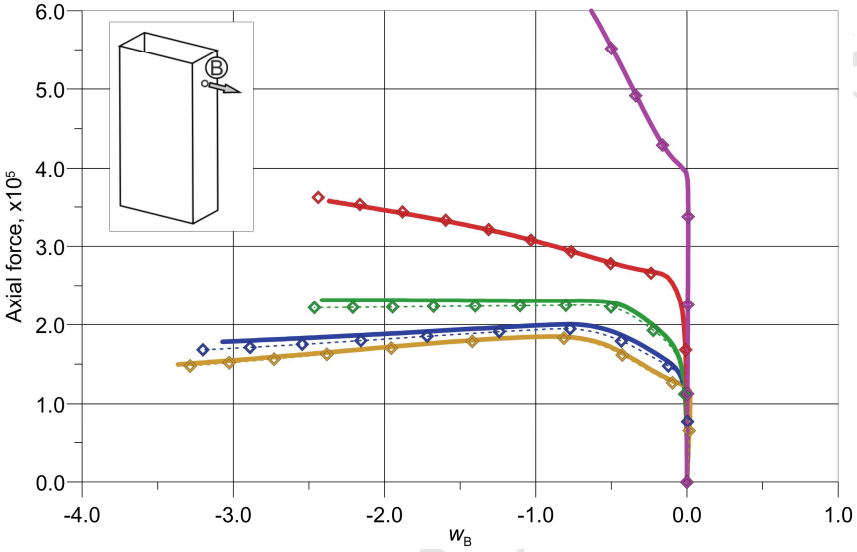

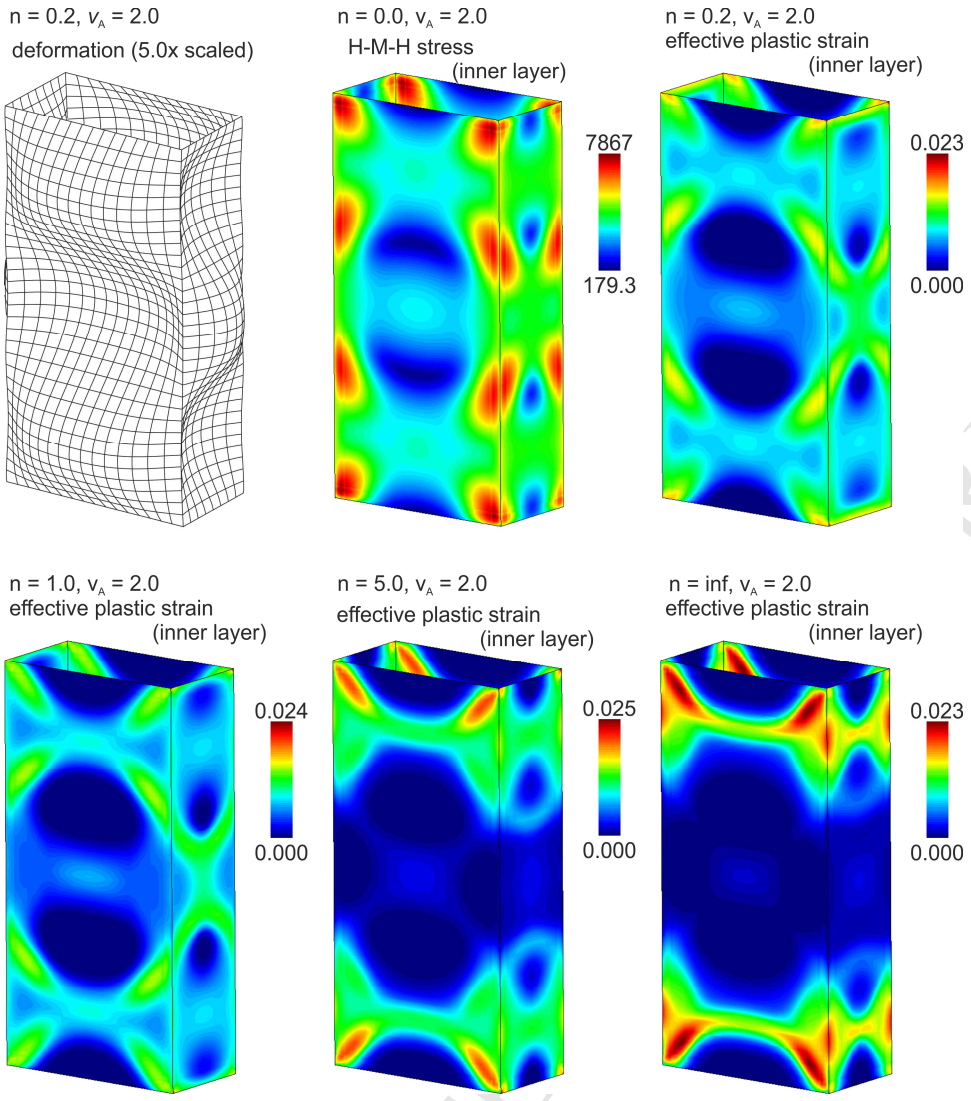

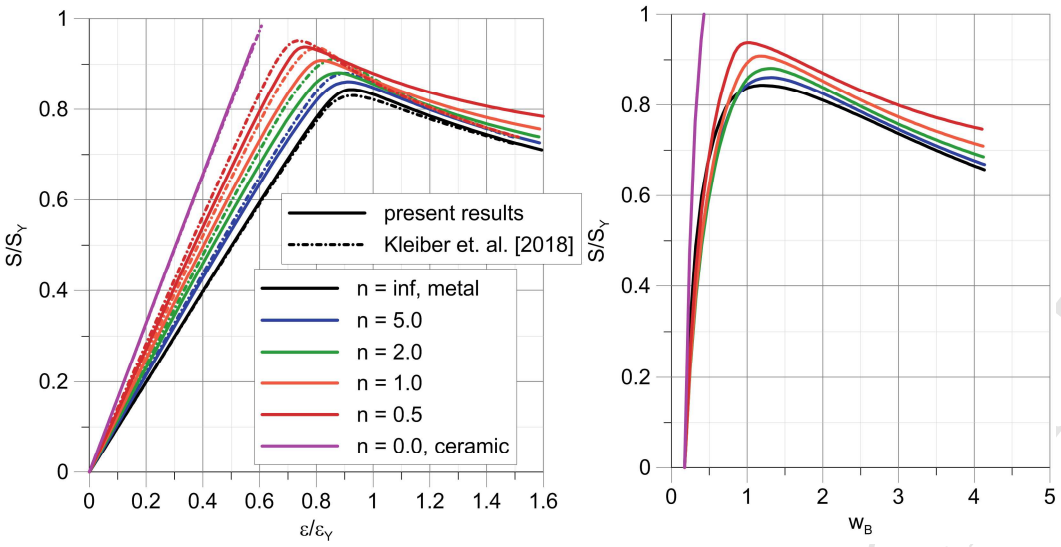

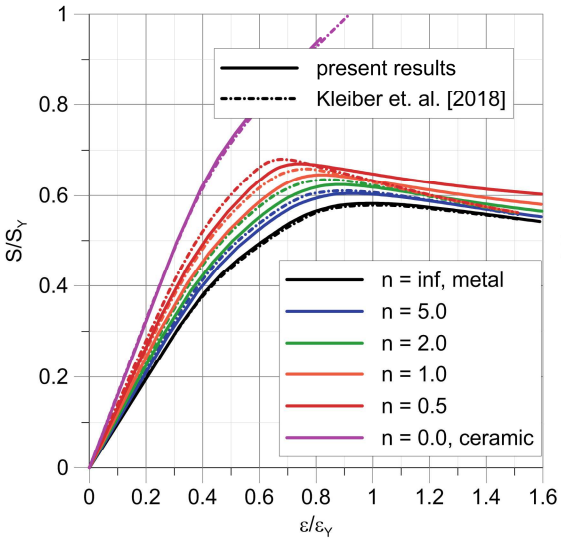

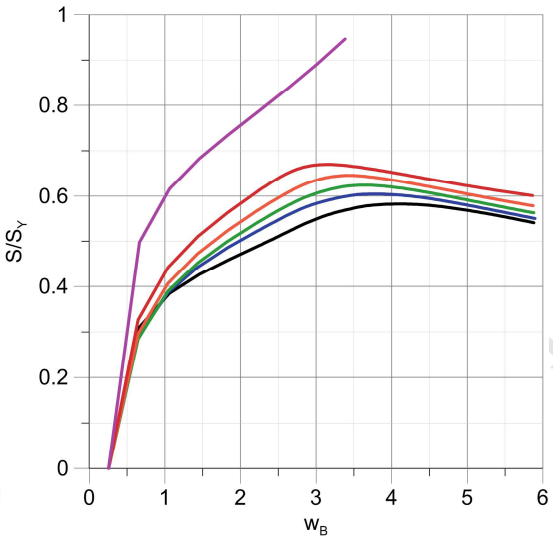

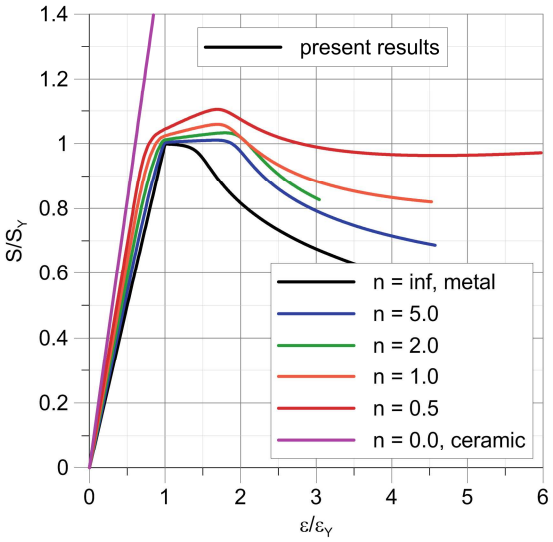

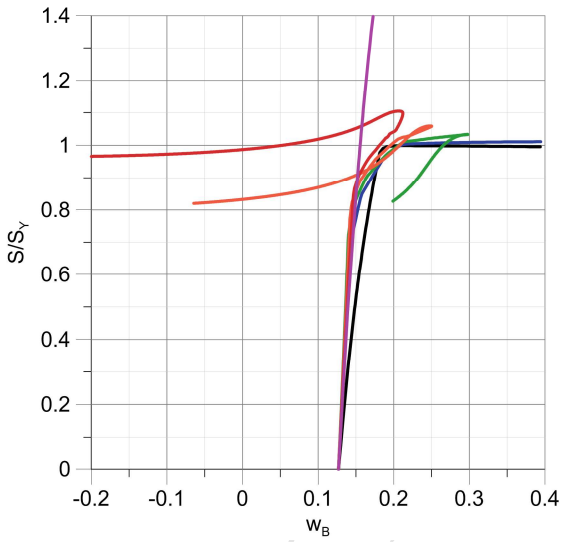

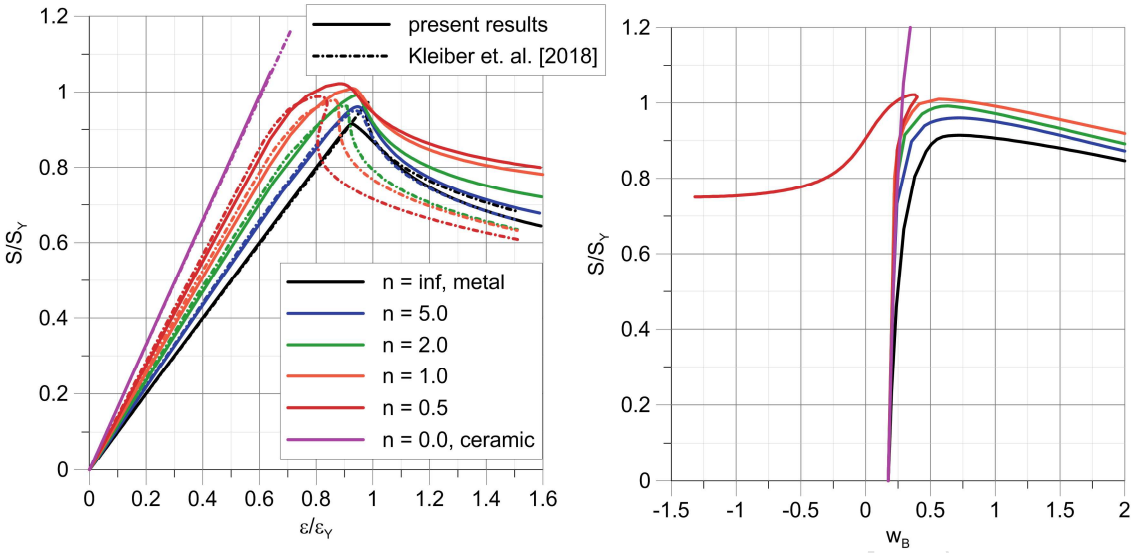

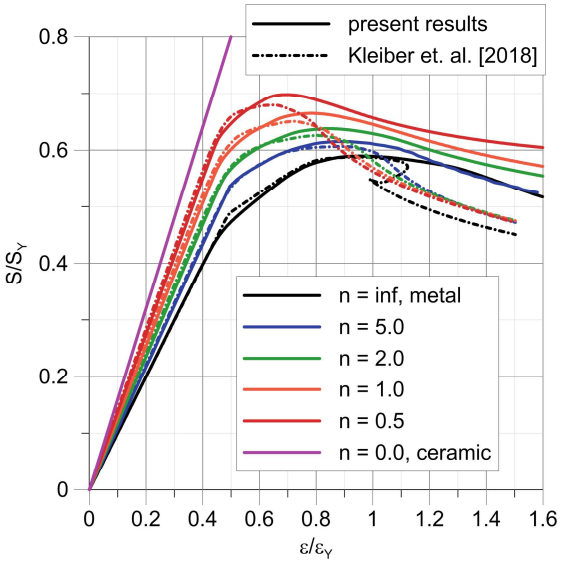

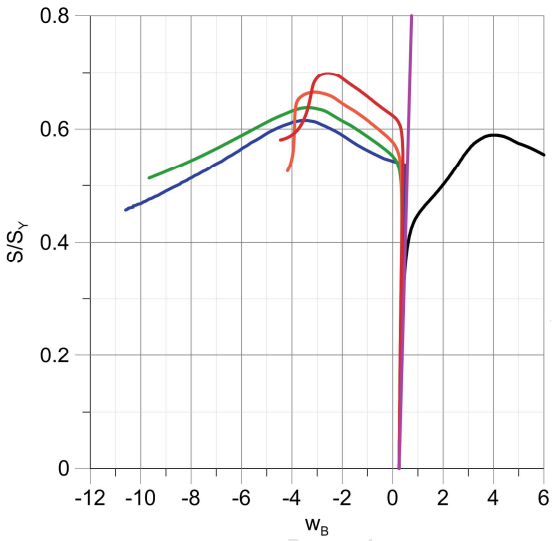

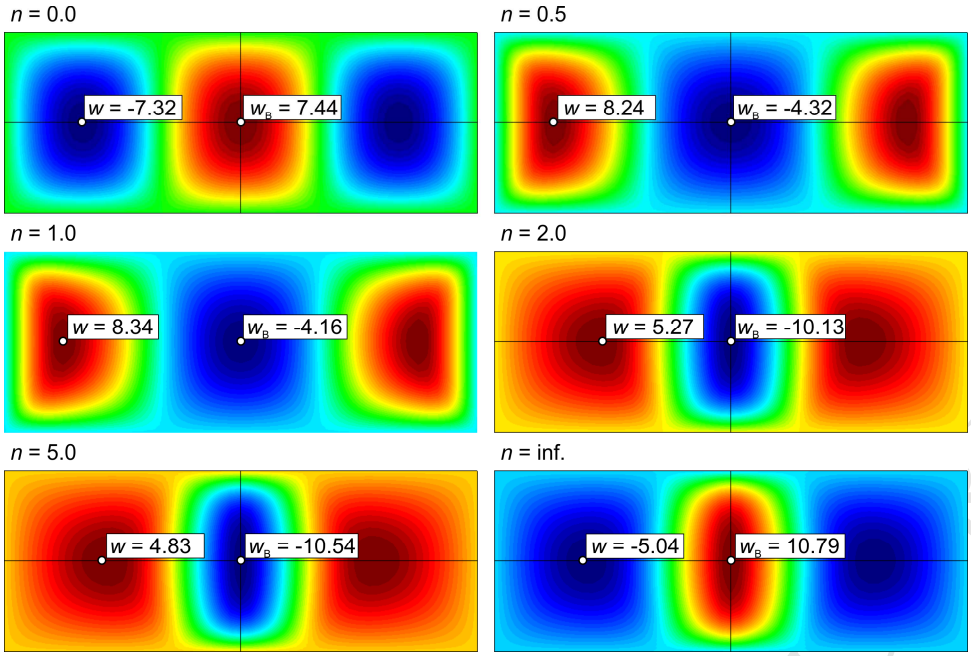

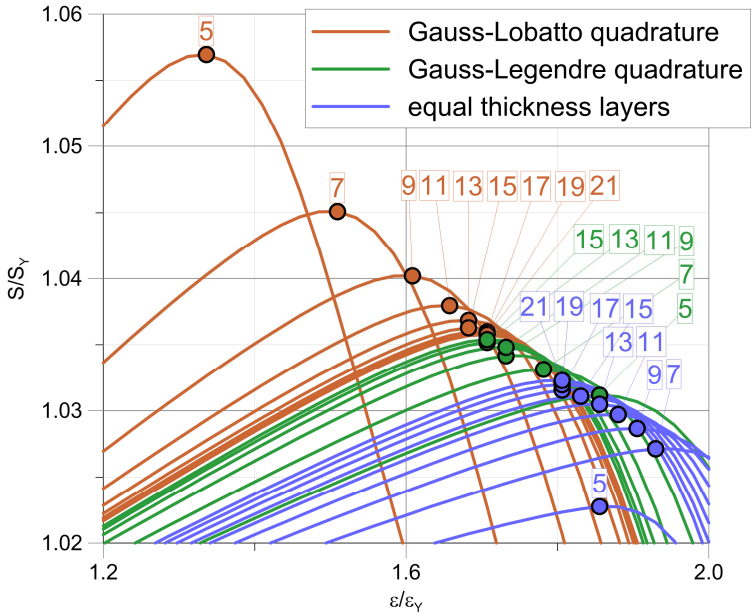

- Standard TTO formulation of elastoplastic functionally graded material is extended to Cosserat type shell theory, with asymmetric membrane strain measures and drilling rotation,
- Numerical results contain vital information about the use of different quadrature rules used to integrate the stress components in the through-the-thickness direction of the shell,
- The influence of finite element discretization and formulation is studied, specifically on the post-peak response of the shell